

Description of Compton peaks in energy-dispersive x-ray fluorescence spectra[†]

M. Van Gysel, P. Lemberge and P. Van Espen*

Micro- and Trace Analysis Centre (MiTAC), Department of Chemistry, University of Antwerp, Universiteitsplein 1, 2610 Antwerp, Belgium

Received 1 March 2002; Accepted 23 September 2002

A new model for the description of incoherent peaks observed in energy-dispersive x-ray fluorescence spectra is proposed. The model was derived after a systematic study of peak shapes based on Monte Carlo simulations. The model consists of a Gaussian modified by two exponential tail functions. The model is implemented in a non-linear least-squares fitting procedure and tested on spectra measured with a ¹⁰⁹Cd excitation XRF setup using an HPGe detector. Copyright © 2003 John Wiley & Sons, Ltd.

INTRODUCTION

A number of quantitative analysis procedures in x-ray fluorescence (XRF) make use of the intensity of scattered radiation to correct for matrix effects and/or the variability of instrumental parameters. Andermann and Kemp¹ were the first to apply this concept for the quantitative analysis of ores using the 'line-to-scatter' ratio. Similar procedures,^{2,3} using the coherent scattered intensity, were developed. In addition, methods using the Compton-to-Rayleigh line ratio were studied.^{4–6} All these methods require that the net intensity of the coherently (Rayleigh) and incoherently (Compton) scattered radiation can be estimated with high accuracy.

Whereas the Rayleigh peak can be described fairly well by a Gaussian with a width corresponding to the spectrometer resolution, similar to the description of the fluorescence lines, the Compton peak is much broader and has a much more non-Gaussian shape. Therefore, spectrum evaluation programs^{7–9} relying on Gaussian peak shapes fail to determine the intensity of the Compton peak. In addition, owing to the partial overlap with the Compton peak, the Rayleigh peak is also difficult to model. The absence of a suitable fitting model led to the use of empirical methods or broadened Gaussians.^{10–14}

The aim of this work was to develop an analytical expression that gives a good approximation of the Compton peak profile under different experimental conditions and to implement this model in a non-linear least-squares procedure for spectrum evaluation, so that net intensities of scattered peaks can be obtained accurately.

THEORY

When an x-ray photon interacts with an atomic electron, it can be absorbed or scattered. Absorption of x-rays gives rise to characteristic x-rays that are emitted isotropically.

Scattering takes place either inelastically (Compton) or elastically (Rayleigh). The energy of an elastically scattered x-ray remains unchanged, while the energy of an incoherently scattered x-ray shifts towards lower values. Considering a free electron at rest, the energy of an inelastically scattered photon is given by the well-known Compton equation:¹⁵

$$\Delta E = \frac{E_0 \cdot E_c}{m \cdot c^2} \cdot (1 - \cos \theta) \quad (1)$$

where ΔE is the energy difference (keV) between the incident and the scattered radiation, mc^2 is the rest-mass energy of an electron (510.996 keV) and θ is the scattering angle. E_0 is the energy of the photon before the scattering event takes place.

Strictly, the equation is not valid in the case of atomic electrons. By taking into account the Doppler shift, due to the relative motions of the scattering body, source of radiation and observer, the Compton equation becomes¹⁶

$$\Delta E = \frac{E_0^2}{m \cdot c^2} \cdot (1 - \cos \theta) + \frac{2 \cdot E_0 \cdot P_x}{m \cdot c} \cdot \sin \frac{\theta}{2} \cdot \cos \psi \quad (2)$$

The first term is the Compton shift [Eqn (1)] and the second term expresses the shift due to the electron motion, where p_x is the electron momentum and ψ is the angle between the direction of the electron and the normal to the scattering plane. DuMond¹⁶ also showed that, since the electron may move in any direction, $\cos \psi$ has values between -1 and $+1$, the width of the incoherent peak may therefore be expressed as

$$4\beta \frac{hc}{E_0} \sin \frac{\theta}{2}$$

where $\beta = p_x/mc$, h is Planck's constant (6.6254×10^{-34} J s) and c is the velocity of the wave (3×10^8 ms⁻¹ in vacuum). The broadening of the Compton peak is due to a combination of Doppler broadening and the scattering over a series of angles.

Probability of scattering

The probability that an x-ray photon is scattered by a free electron into a solid angle $d\Omega$ is expressed by

*Correspondence to: P. Van Espen, Micro- and Trace Analysis Center (MiTAC), Department of Chemistry, University of Antwerp, Universiteitsplein 1, 2610 Antwerp, Belgium.
E-mail: piet.vanespen@ua.ac.be

[†]Presented at the NURT-2001 Symposium, Havana, Cuba.

the differential cross-sections.¹⁷ The Klein–Nishina or the incoherent differential cross-section (barn electron⁻¹ sr⁻¹) is

$$\frac{d\sigma_{\text{KN}}}{d\Omega}(\theta, E) = \frac{r_e^2}{2} \left(\frac{k}{k_0} \right)^2 \left(\frac{k}{k_0} + \frac{k_0}{k} - \sin^2 \theta \right) \quad (3)$$

and the Thomson or coherent differential cross-section (barn electron⁻¹ sr⁻¹) is

$$\frac{d\sigma_{\text{Th}}}{d\Omega}(\theta, E) = \frac{r_e^2}{2} (1 + \cos^2 \theta) \quad (4)$$

where $r_e = e/m_e c^2$, which is the classical electron radius and e and m_e are the charge and the rest mass of the electron, respectively. When the binding energy of an electron becomes important, the scattering cross-sections must be corrected by a factor that takes into account the binding effect of an electron:

$$\frac{d\sigma_{\text{I}}}{d\Omega}(\theta, E) = \frac{d\sigma_{\text{KN}}}{d\Omega}(\theta, E) S(x, Z) \quad (5)$$

$$\frac{d\sigma_{\text{c}}}{d\Omega}(\theta, E) = \frac{d\sigma_{\text{Th}}}{d\Omega}(\theta, E) F^2(x, Z) \quad (6)$$

where $S(x, Z)$ is the incoherent scattering function and $F(x, Z)$ the form factor. When the binding energy increases, $S(x, Z)$ goes to zero while $F(x, Z)$ approaches Z .

Multiple scattering

DuMond¹⁸ was the first to study the multiple scattering. His model, based on scattering by stationary electrons on a sphere, allowed him to calculate the ratio of double to single scattering. Other studies^{19,20} of multiple scattering were based on the use of Monte Carlo simulations. It is observed from the calculations that the ratio of double to single scattering is reduced when the sample thickness is less than the mean free path for a scattering interaction. When dealing with double scatter spectra, the profile may have two clearly separated maximum intensities, located at the single and double scattered energies from stationary electrons. Third- and higher order scatter spectra do not reveal a clear structure.

Monte Carlo procedure

Unfortunately, there is no closed analytical expression available to describe the Compton intensity distribution. Simulations, however, can provide an accurate estimate of this distribution. An important benefit of simulations is that the Compton profile can be studied before it is distorted (broadened) by the detector response function, i.e. 'ideal' spectra are generated. In this work, we used simulation codes, developed in our laboratory and tested extensively on various synchrotron, micro-XRF and standard XRF setups.^{21,22} A detailed description of the Monte Carlo code used in this work can be found in the work of Vincze.²³ During the simulation, each photon trajectory is modeled as a number of straight steps. The step length of each interaction is calculated from the distribution around the mean-free path λ of the photon, which is a function of the energy. The step length is calculated by the Beer–Lambert law:

$$I(x) = I_0 e^{-\mu x} \quad (7)$$

which describes the amount of radiation that is transmitted through a medium of a thickness x ; $I(x)$ and I_0 are the intensity of the radiation after and before the interaction, respectively, and μ is the linear mass-attenuation coefficient.

In Monte Carlo simulations, a random variable x within a range $x_{\min} \leq x \leq x_{\max}$ is calculated by taking the inverse of a normalized cumulative distribution function $F(x)$ from a probability distribution function $f(t)$. The normalized, cumulative distribution function is defined as

$$F(x) = \frac{\int_{x_{\min}}^x f(t) dt}{\int_{x_{\min}}^{x_{\max}} f(t) dt} \quad (8)$$

$x = F^{-1}(R)$, where R is a uniformly distributed random variable between 0 and 1.

Using Eqn (8), the cumulative distribution function for the interaction in the material over a distance S is expressed as

$$F(S) = \frac{\int_0^S I(x) dx}{\int_0^\infty I(x) dx} = 1 - e^{-\mu(E)S} = R(S) \quad \text{and} \quad \times \begin{cases} S \rightarrow 0 & R(S) \rightarrow 0 \\ S \rightarrow \infty & R(S) \rightarrow 1 \end{cases} \quad (9)$$

Since $R(S)$ has a value between 0 and 1, the inversion of the function leads to an expression that allows the calculation of a step length for a given uniform random number R between 0 and 1:

$$S(R) = -\frac{1}{\mu(E)} \ln(1 - R) \equiv -\lambda(E) \ln(1 - R) \quad (10)$$

where $\lambda(E)$ is the mean free path of the x-rays with an energy E in the material.

After each step, a new direction, atom type and a particular photon–matter interaction are chosen by means of random numbers. In the case of scattering, a scattering angle θ is chosen by the inverse of a cumulative distribution function of scattering $F_E(\theta)$. The cumulative distribution function is expressed as

$$F_E(\theta) = \frac{2\pi}{\sigma(E)} \int_0^\theta \frac{d\sigma}{d\Omega}(v, E) \sin v dv \quad (11)$$

and $\theta = F_E^{-1}(R)$. A direct inversion of the expression in Eqn (11) is not possible. The author calculates $F_E(\theta)$ for a given atomic number and energy. After a numerical inversion of $F_E(\theta)$ and by means of a random number R , a scattering angle is selected. For each random number the scattering angle is calculated by a bilinear interpolation. With the use of this interpolation procedure, the author reports for most of the θ range a deviation smaller than 5% and a deviation up to 10% for small scattering angles ($\theta < 20^\circ$) compared with the exact calculation with the probability density function [Eqn (12)] of the scattering angle at various given energies:

$$P(\theta, \theta + d\theta) = f(\theta) \cdot d\theta = \frac{2\pi}{\sigma(E)} \cdot \frac{d\sigma(\theta, E)}{d\Omega} \cdot \sin \theta \cdot d\theta \quad (12)$$

The differential cross-section used in Eqn (11) can be either an incoherent or a coherent differential cross-section. These are given in Eqns (5) and (6). All values for the incoherent scattering functions $S(x, Z)$ and the atomic form factors $F(x, Z)$ are taken from Hubbell *et al.*¹⁷

Non-linear least-squares regression

To describe spectra by a mathematical function, a least-squares regression technique^{9,24} is used. In general, a function or a fit model $y(x, a_1, \dots, a_n)$ with n parameters a describes an experimental set of data (e.g. spectrum) (x_i, y_i) . The aim of the regression is to find an optimum set of parameters to make the agreement between the experimental data and the theoretical model as high as possible. By taking the chi-square to minimize the difference between experiment and theory, we assume that all residuals $R_i = [y_i - y(x_i, a)]/\sigma_i$ are independent, identical distributed random variables with mean zero and unit variance. During the fitting procedure the chi-square is minimized by modifying the parameters a iteratively.

EXPERIMENTAL

Spectra were simulated for a set of samples in the range $Z = 6$ (C) to $Z = 73$ (Ta) assuming excitation with monochromatic x-rays of 22.163 keV (Ag $K\alpha_1$). All samples were assumed to have a thickness of 0.3 cm (infinitely thick). The number of events considered in each simulation was 1×10^7 and up to four photon-matter interactions were allowed. Scattering events of order 1–4 were stored separately so that their contribution could be estimated individually and studied in detail. The geometric parameters of the simulation are incident and take-off angle of 45° , source-sample and sample-detector distances of 3 cm, an opening angle of 8° to account for the beam divergence and a detector area of 1 cm^2 . Vacuum is considered in the excitation chamber. A typical simulation on a Pentium III 450 MHz computer takes 30 min. Figure 1 shows the 'ideal' (unconvoluted) spectrum of the scattered radiation from carbon, iron and tin samples.

To evaluate this fitting model with experimental data, a number of NIST standard reference materials (SRMs), a cellulose pellet and a few compounds with an average Z covering the range 6–50 were measured.

The compounds (p.a.) were placed in a SPEX cup (40 mm X-Cell; CertiPrep, USA) with a Mylar window ($3 \mu\text{m}$; CertiPrep). All spectra were collected using a portable XRF system (Canberra portable XRF system) equipped with a ^{109}Cd isotope source and an HPGe detector (100 mm^2 , $\sim 160 \text{ eV}$ FWHM). All spectra were measured for 1000 s in air.

RESULTS AND DISCUSSION

Evaluation of the incoherent peak shape

For low- Z elements, the multiple scatter events contribute significantly. One also observes that the multiple scattering events produce a photon distribution that extends towards lower energy. The intensity of the various Compton contributions was obtained by a simple numerical integration

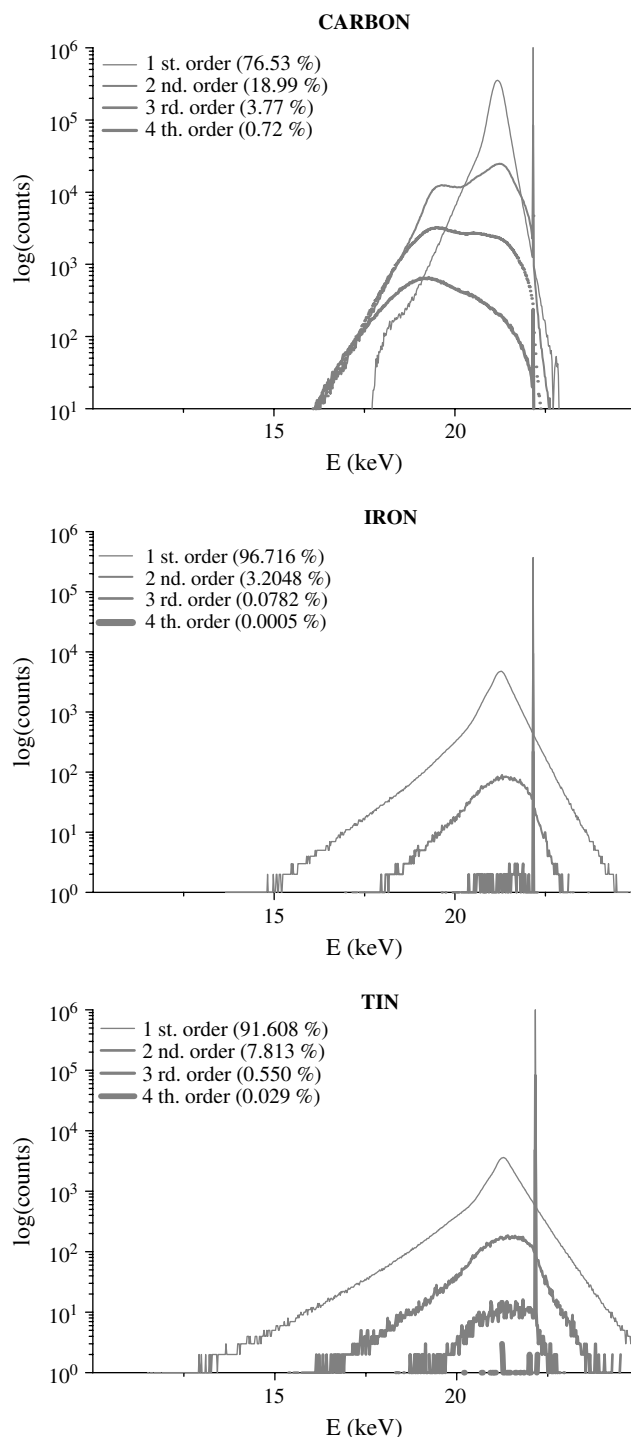


Figure 1. Simulated scatter events in carbon ($Z = 6$), iron ($Z = 26$) and tin ($Z = 50$) excited with Ag $K\alpha_1$ x-rays. The profile due to the first- to fourth-order Compton scattering and contribution of the Rayleigh peak are shown.

of these profiles (after subtraction of the Rayleigh peak). Figure 2 shows the relative contribution of the single and double Compton scattering. Especially for low- Z elements, multiple Compton scattering is significant. In the case of carbon, double Compton scattering comprises 18% and triple scattering 3% of all scattering events. For intermediate- Z elements (P to Fe), the contribution of multiple scattering is below 10%. In the region $Z = 40$ –50 a discontinuity

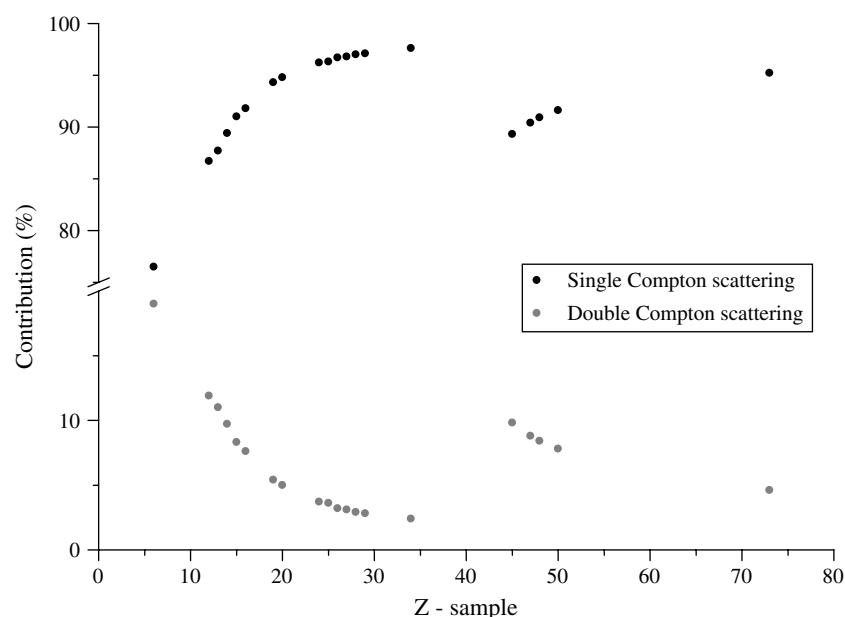


Figure 2. Relative contribution of single and double Compton scattering interactions at 22.163 keV as a function of the atomic number of the sample. Note the discontinuity in the region $Z = 40\text{--}50$.

is observed due to the variation of photoelectric absorption with atomic number at the given energy (22.163 keV). For elements below Ru ($Z = 44$), photoelectric absorption takes place in both the K and L shells, from Ru on, only the L shell is involved ($E_{K_{ab}}$ 22.12 keV). As a result, the mass attenuation coefficient is lower, resulting in a deeper penetration of the primary radiation and more multiple scattering.

Investigation of a fit model

The simulated spectra were used in order to develop an analytical expression to model the scatter profile. Because multiple scatter profiles have a very complex structure and a relatively small contribution, we limited ourselves to the description of the single scatter profile. Before the simulated spectra can be used, the broadening due to the finite resolution of the solid-state detector needs to

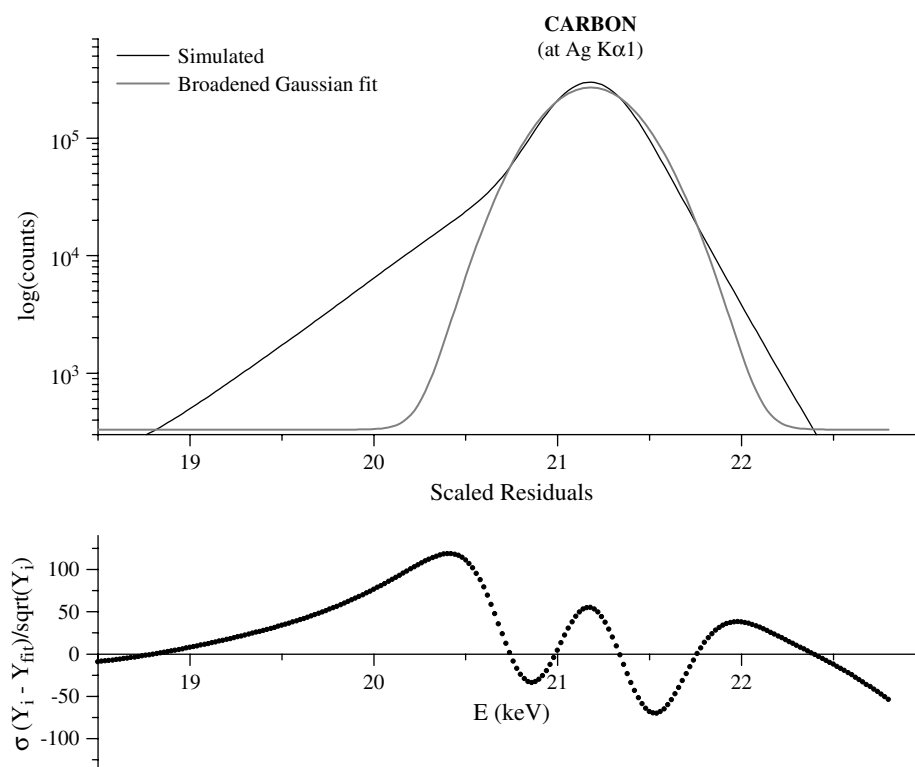


Figure 3. A Compton profile fitted by a broadened Gaussian. The residuals of fit show a clear structure at the high- and low-energy sides of the peak.

be taken into account. This was done by convoluting the simulated spectra with a Gaussian detector response function, assuming a gain of 20.0 eV per channel, a noise contribution of 100.0 eV (FWHM) and a Fano factor of 0.114. The spectra obtained in this way were used to test various fitting functions. From Fig. 3, it is clear that a simple broadened Gaussian, with a width beyond the spectrometer resolution at that energy, is incapable of describing a single scattering Compton profile. Other functions, such as a combination of a few (broadened) Gaussians, a Lorentzian and the convolution of a Gaussian and a Lorentzian (i.e. Voigt profile), all gave a very poor performance. The residuals of fit clearly demonstrate the presence of a low- and a high-energy tail of different magnitude. Since the tails are linear on a semi-logarithmic scale, it was decided to add exponential tails to the description of the Compton peak. An exponential function convoluted with a Gaussian results in an exponential function multiplied with an error function complement. Thus the tail function, in its most general form, can be written as

$$T(\Delta E) = \frac{\text{Gain}}{2\gamma\sigma e^{-\frac{1}{2\gamma^2}}} e^{\frac{\Delta E}{\gamma\sigma}} \text{erfc}\left(\frac{\Delta E}{\sqrt{2}\sigma} + \frac{1}{\sqrt{2}\gamma}\right) \quad (13)$$

The first term, including an exponential function in the denominator, is a normalization factor, so that the integral is unity. ΔE is defined as the energy at channel i minus the energy of the peak to be modeled. In the literature, similar tail functions^{25–27} are used to model the characteristic peaks. Using this function [Eqn (13)], the low-energy side (T_A) can be described. In order to include the high-energy tailing (T_B), a transformation has to be carried out:

$$T_B = T_A(-\Delta E) \quad (14)$$

A similar expression is also used in the description of high-energy tailing of characteristic peaks.²⁸

In Eqn (13), σ is defined as the resolution of the spectrometer in sigma units and γ determines the slope of the tail function (or width). Gain expresses the energy interval (eV) per channel.

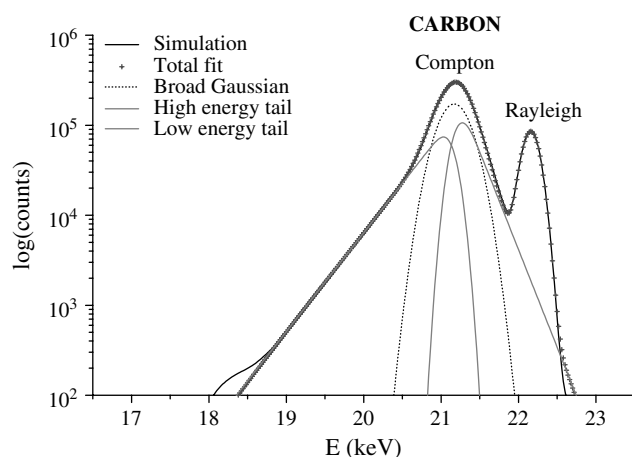


Figure 4. Fit of a convoluted, simulated spectrum using a Gaussian with two exponential tails [Eqn (16)]. Sample: carbon. Primary photons: 22.163 keV.

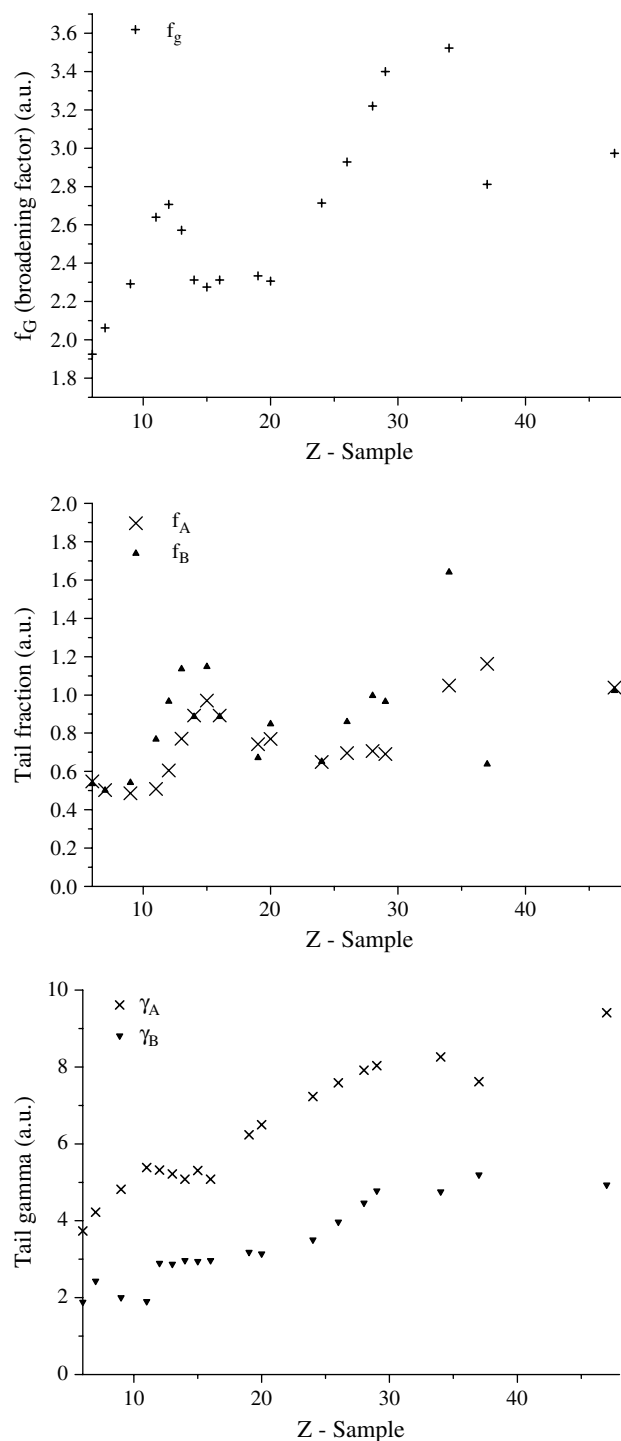


Figure 5. Fitted Compton peak parameters as function of the atomic number of the sample. Top, broadening factor; middle, tail fraction; bottom, tail gamma.

A fitting function for a Compton peak can be expressed as

$$y(i) = G_c(\Delta E) + f_A T_A(\Delta E) + f_B T_B(\Delta E) \quad (15)$$

where G_c is a Gaussian which is broadened by multiplying σ by a factor f_G (see below). Each tail function is multiplied with a tail fraction, which is expressed as a fraction of the Gaussian contribution. A Compton peak observed in a real spectrum consists of $K\alpha$ and $K\beta$ peaks each with various lines of slightly different energies ($K\alpha_1$, $K\alpha_2$, etc.).

Therefore, the entire Compton peak (group) is described in the following way:

$$y(i) = \sum_{j=1}^{np_g} A_j \left\{ \sum_{k=1}^{np(j)} R_{jk} [G_c(\Delta E) + f_A T_A(\Delta E) + f_B T_B(\Delta E)] \right\} \quad (16)$$

where A_j is the total area of a peak group j (e.g. $K\alpha$) and R_{jk} is the relative intensity of each line k of a peak group j . The energy $E_{c,jk}$ is calculated according to the well-known Compton equation [Eqn (1)]. The sum over j takes into account np_g peak groups and the sum over k takes into account the np peaks within a peak group j .

The functions G_c , T_A and T_B used in Eqn (16) are expressed as

$$G_c(\Delta E) = \frac{\text{Gain}}{\sqrt{2\pi}\sigma_{c,jk}f_g} e^{-\frac{1}{2}\left(\frac{\Delta E}{\sigma_{c,jk}f_g}\right)^2} \quad (17)$$

$$T_A(\Delta E) = \frac{\text{Gain}}{2\gamma_A\sigma_{c,jk}} e^{-\frac{1}{2\gamma_A^2}} e^{\frac{\Delta E}{\gamma_A\sigma_{c,jk}}} \text{erfc}\left(\frac{\Delta E}{\sqrt{2}\sigma_{c,jk}} + \frac{1}{\sqrt{2}\gamma_A}\right) \quad (18)$$

$$T_B(\Delta E) = \frac{\text{Gain}}{2\gamma_B\sigma_{c,jk}} e^{-\frac{1}{2\gamma_B^2}} e^{-\frac{\Delta E}{\gamma_B\sigma_{c,jk}}} \text{erfc}\left(\frac{-\Delta E}{\sqrt{2}\sigma_{c,jk}} + \frac{1}{\sqrt{2}\gamma_B}\right) \quad (19)$$

with

$$\Delta E = E(i) - E_{c,jk}$$

$$\sigma_{c,jk} = \left[\left(\frac{\text{Noise}}{2\sqrt{2\ln 2}} \right)^2 + \varepsilon \text{Fano} E_{c,jk} \right]^{1/2} \quad (20)$$

$$E(i) = \text{Zero} + \text{Gain} \times i \quad (21)$$

$\sigma_{c,jk}$ describes the spectrometer resolution at energy $E_{c,jk}$ and $E(i)$ is defined as the energy at channel i ; ε is the average required to create an electron-hole pair (Ge: 3.04 eV).

The Compton peak model [Eqn (16)] was implemented in a non-linear least-squares procedure⁹ in which the following parameters are estimated: the net intensity of each peak (fluorescent and scattered), the Compton parameters f_A , f_B , γ_A , γ_B , f_G , $E_{c,jk}$, the calibration (Zero, Gain, Noise and Fano) and the continuum parameters. Since monochromatic radiation was used, a linear background model was applied in all calculations. The escape peaks from Ge with a $K\alpha$ escape at $E_{c,jk} - 9.875$ keV and a $K\beta$ escape at $E_{c,jk} - 10.981$ keV are given the same parameters as the parent peak. Figure 4 shows a fitted profile of a simulated spectrum of a carbon sample.

The parameters γ_A , γ_B , $E_{c,jk}$ and f_G , f_A , f_B were determined and evaluated against the atomic number (Fig. 5) for a set of simulated profiles (convoluted) in a range $Z = 6$ (C) to $Z = 47$ (Ag). By making use of the determined parameters, the fitting of real spectra can be initialized in a more reliable way.

From Fig. 5, clear trends can be observed. The width of the Compton profile increases with increasing atomic number. This trend is expected since the binding energy or electron momentum becomes important at higher atomic numbers. The relative contribution of the tailing [Eqn (22)] at higher Z elements increases (from 26 to 33%), while the contribution of the Gaussian decreases (from 49 to 32%) because of a larger region in which scattering occurs (Fig 1). The relative contribution of the tailing is defined as

$$R_{f_A}(\%) = \frac{f_A}{f_A + f_B + 1} \times 100 \quad (22)$$

where f_A , f_B and 1 are the contributions, with respect to the Gaussian area, of the low-energy tail, high-energy tail and the broadened Gaussian, respectively.

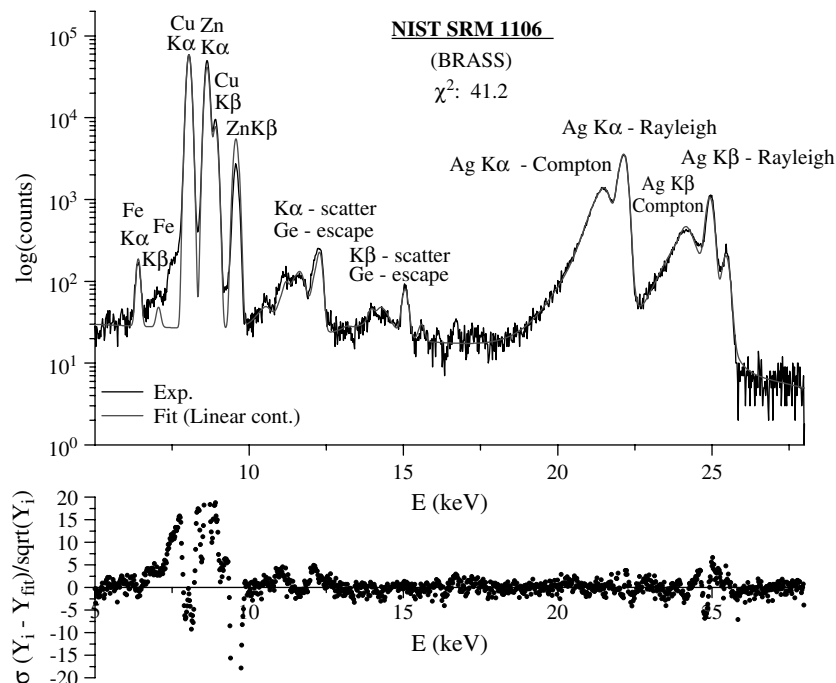


Figure 6. A fitted spectrum of a NIST SRM 1106 standard reference material using the Compton peak model on a linear continuum.

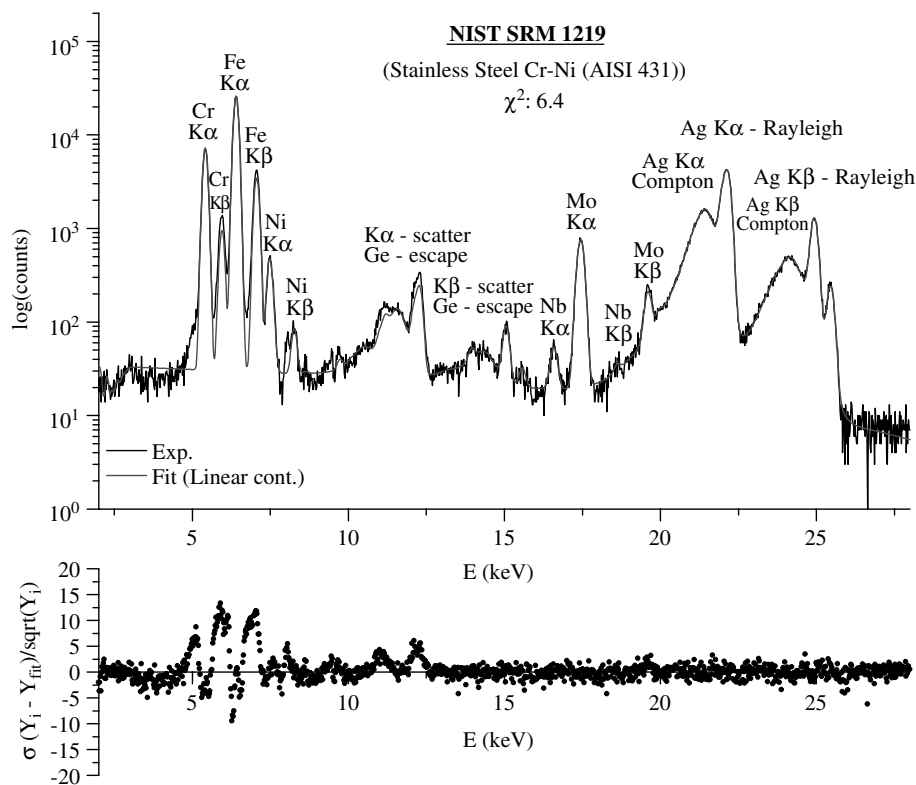


Figure 7. A fitted spectrum of a NIST SRM 1219 standard reference material using the Compton peak model on a linear continuum.

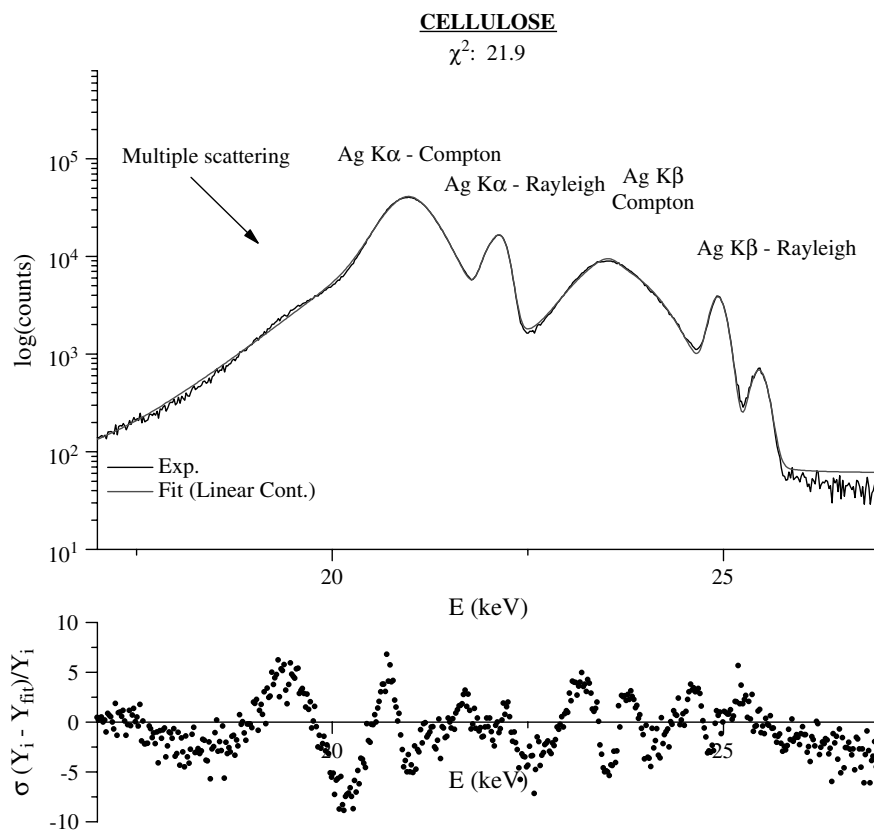


Figure 8. Compton profiles of a cellulose sample. The multiple scatter contribution around 19 keV is not modeled by the fitting function.

Table I. Compton peak parameters for real spectra

	Sample	$\langle Z \rangle$	f_G	f_A	f_B	γ_A	γ_B	χ^2
Compton Ag $K\alpha$	Carbon	6	3.12	0.67	0.31	7.76	5.20	37.87
	Cellulose	6.7	3.23	0.80	0.49	7.19	4.88	21.99 ^a
	H ₃ BO ₃	7.13	3.61	0.63	0.21	7.11	3.37	8.91
	KMnO ₄	16.63	4.22	0.46	0.29	7.44	3.93	3.26
	NIST SRM1219	25.64	3.66	0.86	0.32	6.37	2.19	6.40
	NIST SRM1154	25.8	3.74	0.66	0.31	8.40	2.45	9.78
	NIST SRM629	29.09	3.30	1.03	0.49	5.77	2.07	58.37 ^b
	NIST SRM1106	29.52	3.50	0.77	0.24	5.74	0.94	41.20 ^c
Compton Ag $K\beta$	Carbon	6.0	4.69	0.16	0.03	3.28	1.07	
	Cellulose	6.7	4.82	0.28	0.08	3.99	3.55	
	H ₃ BO ₃	7.13	4.84	0.43	0.11	7.28	3.59	
	KMnO ₄	16.63	5.69	0.09	0.04	10.33	0.71	
	NIST SRM1219	25.64	4.93	0.68	0.19	8.01	2.45	
	NIST SRM1154	25.8	5.12	1.19	0.42	7.30	3.09	
	NIST SRM629	29.09	4.53	1.47	0.89	6.05	2.80	
	NIST SRM1106	29.52	5.32	1.37	1.50	4.93	2.83	

^a A large discrepancy due to the escape peaks (not shown in the spectrum) ($+15\sigma$).

^b Sum peak at 17 keV ($+10\sigma$) and characteristic peak tailing ($+30\sigma$) not included.

^c Large deviations ($+20\sigma$) at the characteristic lines (fitted as one group and no peak tailing included).

Experimental evaluation of the fit model

The fitting model applied to simulated spectra seems to work well. In Fig 6–8 the measured and fitted spectra of NIST SRM 1106, NIST SRM 1219 and cellulose are shown. The Compton and the Rayleigh region is fitted very well with residuals not exceeding $\pm 5\sigma$. Also the scatter escape peaks are modeled with sufficient accuracy. The discrepancies observed for the fluorescence lines are due to the fact that in this work only simple Gaussians were used to model these lines. In Table 1 the experimental Compton parameters are shown. Comparing the parameters determined from the simulations with those obtained experimentally, we note that there is good agreement. However, the tailwidths are in less agreement owing to detector broadening and overlap with characteristic peaks. In the case of low- Z samples, the multiple scattering broadens the low-energy side of the profile to a great extent.

In the spectra of NIST SRM 1154 and NIST SRM 1219, strong interference of Mo and Nb K peaks and the $K\alpha$ Compton occurs, but still a good fit is achieved. In the residuals of low- Z spectra one also observes multiple scattering contributions, as shown in the spectrum measured for a cellulose sample (Fig. 8). In this figure the multiple scatter contribution around 19.0 keV is indicated.

CONCLUSIONS

Making use of the benefits of a Monte Carlo simulation, we derived systematically an analytical expression to model incoherent peak shapes. A model was constructed based on a simulated set of single scatter peaks. Despite the fact that multiple scattering may be significantly present, a good description in fitting real spectra was obtained. It

was also observed that there is good agreement between the experimentally determined Compton parameters and those obtained from simulated spectra. Finally, the peak model was tested on real spectra and excellent fits were achieved. In future work, a complete fit model will be investigated to model both characteristic and scatter peaks accurately.

REFERENCES

1. Andermann G, Kemp JW. *Anal. Chem.* 1958; **30**: 8.
2. Kalman ZH, Heller LH. *Anal. Chem.* 1962; **34**: 8.
3. Cullen TJ. *Anal. Chem.* 1962; **34**: 7.
4. Dwiggins CW Jr. *Anal. Chem.* 1961; **33**: 1.
5. Johnson CM, Stout PR. *Anal. Chem.* 1923; **30**: 12.
6. Klunder H. Dissertation, Rijksuniversiteit Utrecht, 1970.
7. Van Espen P, Nullens H, Adams F. *Nucl. Instrum. Methods* 1977; **142**: 243.
8. Van Espen P, Nullens H, Adams F. *Nucl. Instrum. Methods* 1977; **145**: 579.
9. Van Espen P, Janssens K. In *Handbook of X-Ray Spectrometry*, Van Grieken R, Markowicz R (eds). Marcel Dekker: New York, 1992; Chapt 4, 186.
10. Domi N. *X-Ray Spectrom.* 1992; **21**: 163.
11. Renault J. *Adv. X-ray Anal.* 1980; **23**: 45.
12. Matsuura N, Kurozumi S, Fukuzaki T, Arai T. *Adv. X-Ray Anal.* 1993; **36**: 111.
13. Swoboda W, Beckhoff B, Kanngieser B, Scheer J. *Adv. X-Ray Anal.* 1994; **37**: 667.
14. Van Espen P, Van't Dack L, Adams F, Van Grieken R. *Anal. Chem.* 1979; **51**: 961.
15. Compton AH, Allison SK. *X-Rays in Theory and Experiment*. Van Nostrand: New York, 1967; chapt. III.
16. DuMond JWM. *Rev. Mod. Phys.* 1933; **5**: 1.
17. Hubbell JH, Veigele WJ, Briggs EA, Brown RT, Cromer DT, Howerton RJ. *J. Phys. Chem. Ref. Data* 1975; **4**: 471.
18. DuMond JWM. *Phys. Rev.* 1930; **36**: 1685.
19. Halonen V, Williams BG, Paakkari T. *Phys. Fenn.* 1975; **10**: 107.
20. Van Dyck P, Torok S, Van Grieken R. *X-Ray Spectrom.* 1986; **15**: 231.

21. Vincze L. *Spectrochim. Acta, Part B* 1995; **50**: 12.
22. Vincze L, Janssens K, Vekemans B, Adams F. *Spectrochim. Acta, Part B* 1999; **54**: 1711.
23. Vincze L. Dissertation, University of Antwerp, 1995.
24. Marquardt DW. *J. Soc. Ind. Appl. Math.* 1963; **11**: 431.
25. Campbell JL, Perujo A, Millman BM. *X-Ray Spectrom.* 1987; **16**: 195.
26. Campbell JL, Wang JX. *X-Ray Spectrom.* 1991; **20**: 191.
27. Lemberge P. Dissertation, University of Antwerp, 2000; chapt. V.
28. Phillips GW, Marlow KW. *Nucl. Instrum. Methods* 1976; **137**: 525.